

Article

# Hovering Flight of a Robotic Hummingbird: Dynamic Observer and Flight Tests

Han Wang , Yousef Farid , Liang Wang , Emanuele Garone  and André Preumont \* 

Department of Control Engineering and System Analysis, Université Libre de Bruxelles (ULB), CP. 165-55, 50 Av. F.D. Roosevelt, B-1050 Brussels, Belgium; han.wang@ulb.be (H.W.); yousef.farid@ulb.be (Y.F.); liang.wang@ulb.be (L.W.); emanuele.garone@ulb.be (E.G.)

\* Correspondence: andre.preumont@ulb.be

**Abstract:** The paper reports on flight tests at hovering of the *COLIBRI* robot. After a short review of the control model and the stabilization strategy, two different approaches are considered for the attitude reconstruction from the MEMS Inertial Measurement Unit (IMU): the complementary filter and the full-state dynamic observer, implemented in a specially designed flight control board. It is shown that both strategies provide adequate stabilization at hovering in spite of the strong vibration excitation resulting from the flapping of the wings. Moreover, it is shown that the residual wandering due to noise, robot imperfection, etc., can be significantly reduced by a cascade control loop based on the axial and lateral velocities reconstructed by the full-state observer. Experiments show that this approach based on onboard measurements allows for a station keeping as good as that obtained with velocities reconstructed from an external tracking system. The paper also reports endurance tests conducted with two different robot configurations; the maximum flight time observed is 4 min 30 s.

**Keywords:** hummingbird; COLIBRI; hovering flight; full-state dynamic observer; IMU; attitude reconstruction; complementary filter; Kalman filter; flapping noise



**Citation:** Wang, H.; Farid, Y.; Wang, L.; Garone, E.; Preumont, A. Hovering Flight of a Robotic Hummingbird: Dynamic Observer and Flight Tests. *Actuators* **2024**, *13*, 91. <https://doi.org/10.3390/act13030091>

Academic Editor: Zhuming Bi

Received: 4 February 2024

Revised: 21 February 2024

Accepted: 26 February 2024

Published: 27 February 2024



**Copyright:** © 2024 by the authors. Licensee MDPI, Basel, Switzerland. This article is an open access article distributed under the terms and conditions of the Creative Commons Attribution (CC BY) license (<https://creativecommons.org/licenses/by/4.0/>).

## 1. Introduction

Mankind has always been fascinated by the agility of small birds and the hummingbird in particular, which is the only one capable of hovering, flying backward and sideways. In the past decade, miniature components (electronic components, MEMS inertial units, high energy-density batteries) have become available, leading to various research projects involving robotic hummingbirds. The problem is difficult, because it involves many different fields such as unsteady aerodynamics, aeroelasticity, mechanism, manufacturing and control. Not many academic projects went as far as flying. An excellent review of ongoing studies in the field of flapping-wing micro air vehicles is available in [1] (see also [2]). Particularly relevant are the impressive Nanohummingbirds [3], developed by Aeroenvironment with DARPA funding, and the Konuk university robot [4,5], with a weight of only 15.8 g and a flight autonomy of 9 min.

Our project named *COLIBRI* is tailless with two membrane wings, of the size of a large hummingbird. A general view of the robot is presented in Figure 1; the left side shows an early version of the robot [6–8] with the control board on top of the robot [9]. The right side shows the current configuration where the control board and the two batteries are located at the bottom of the robot. The wing span is 21 cm, the flapping frequency is 20 Hz and the weight is around 22–23 g depending on the configuration. The flapping mechanism and gearbox are documented in [10]. The wings consist of membranes attached to the leading edge bars (moved by the flapping mechanism) and the control bars used to change the membrane wings configuration in order to generate the control torques (the technique called *wing twist modulation* was pioneered in [3]). All actuators (motor, servos) are low-cost, off-the-shelf components. The robot structure is 3-D printed. The initial version of the

COLIBRI robot used a Micro MWC Flight Control Board of Hobbyking with a clock of 16 MHz and a six-axes IMU (three gyro axes and three accelerometer axes), for a weight of 1.8 gr. A new control board has been developed including a ARM processor with a clockspeed of 168 MHz and two IMU sensors, one with six axes and one with nine axes, including a magnetometer. The board also includes a Bluetooth link, for a total weight of 1.4 gr; it is briefly described in [11]. The IMUs are particularly critical components in view of the noisy environment due to the flapping of the wings; the flapping noise is analysed in [11].

It is not difficult to imagine the wide range of applications that a robotic hummingbird could perform if it were available with an agility comparable to that of real birds, particularly the most difficult task of all: reconnaissance in a confined, unstructured environment. On the military side, drones are taking an increasing role in modern warfare; robotic birds would bring the highly desirable feature of concealment (camouflage). But prior to this, one must produce a robot capable of following a trajectory with reasonable accuracy for a sufficient flight time (for comparison, the *Black Hornet*, a rotorcraft of the size of a small bird popular in the military, has a flight autonomy of 25 min, and a price tag of six digits). The current limit to autonomy is that the mass of existing robotic hummingbirds is still about twice the mass of their natural counterpart with the same wing span [12].

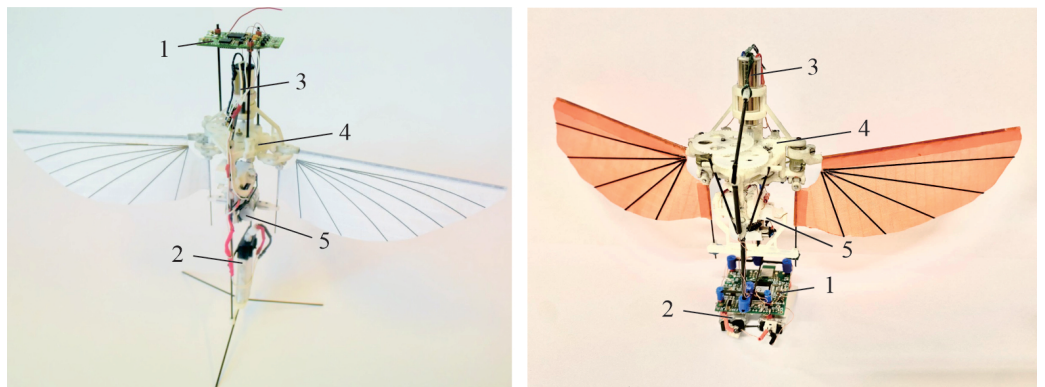


**Figure 1.** The robot COLIBRI. Left: early version with the control board on top [7]. Right: current configuration with the control board at the bottom. (1) Flight control board, (2) batteries, (3) main motor, (4) gearbox and flapping mechanism, (5) attitude control actuators.

The MEMS inertial unit (IMU) of a flapping wing robot is a critical component because of the intense flapping noise; this motivated researchers to provide the control board with two different IMUs with different full-scale ranges. Each of them consists of three rate gyros measuring the roll-pitch-yaw angular velocity in the robot frame and the three components of the *specific acceleration*  $\mathbf{s} = \mathbf{a} - \mathbf{g}$  (the absolute vector acceleration  $\mathbf{a}$  of the IMU unit minus the gravity vector  $\mathbf{g}$ ). In hovering,  $\mathbf{a} = 0$  and the specific acceleration  $\mathbf{s} = (s_x, s_y, s_z)^T$  indicates the position of the gravity vector in the robot frame, from which the robot attitude (roll-pitch) can (in principle) be calculated. However, the acceleration and angular velocity data are subject to intense flapping noise at the flapping frequency and higher harmonics (the harmonic content of the lift and drag forces and the aerodynamic torque is documented in [11], together with a brief description of the control board).

At hovering, the dynamics of the pitch and roll axes of a robotic hummingbird are unstable; they can be stabilized actively if the robot attitude and angular velocities are available (or can be reconstructed) from the IMU. If the pitch and roll references are set to 0, the robot will inevitably drift from the starting position and an additional sensor is required for station keeping (on-board optical flow sensor or external sensor such a video external attitude tracking system). The present study explores an alternative approach based on a dynamic state observer reconstructing the linear forward and lateral velocities.

The present paper is organized as follows: Section 2 briefly recalls the equations governing the cycle-averaged longitudinal and lateral flight dynamics of the robot (they

are essentially the same as those used in the simulation paper). Section 3 discusses the feedback stabilization with a PD compensator, assuming a perfect knowledge of the pitch angle  $\theta$  and pitch rate  $q$ . While the pitch rate is directly available from the gyro, the pitch attitude angle is not. Section 4 considers two different strategies for attitude reconstruction: complementary filter and full-state (Luenberger) observer; both strategies are successful in stabilizing the robot in spite of the strong flapping noise, as reported in the flight tests, Section 5. Additionally, because of the availability of an estimator of the axial velocity  $\hat{u}$  in the full-state observer, a PI velocity feedback outer loop significantly improves the station keeping of the hovering robot, with an accuracy comparable with that of earlier tests carried out with an external motion tracking system [6]. Section 6 reports on endurance flights with two different versions of the robot.

## 2. Flight Dynamics

### 2.1. Cycle-Averaged Longitudinal Dynamics

Previous studies have shown that, near hovering, the low-frequency dynamics of the hummingbird robot (say, below 10 Hz) can be modelled as a rigid body and that the weak coupling between the longitudinal (pitch) and the lateral (roll) dynamics allows to treat them as independent. The following discussion will be focused on the longitudinal dynamics; a similar treatment applies to the lateral dynamics (with appropriate values of the model parameters). Since the flapping frequency is high compared to the robot dynamics, the complexity of the aerodynamic forces acting on the robot can be ignored and they may be approximated by their cycle-averaged values; a similar approach was followed by [13–15]. The rapid change in the aerodynamic moment as well as the lift and drag forces during a flapping cycle will appear as noise. Note that, if the aerodynamic forces along the lateral axis are self-balanced within a flapping cycle (due to left-right symmetry), it is not the case in the longitudinal axis, resulting in a significant pitch torque noise and drag forces. To alleviate this, Delft university has developed a flapper drone with four wings [16] which is also self-equilibrated in the longitudinal axis; this architecture increases the lift with the so-called *clap and fling* mechanism and it considerably reduces the flapping disturbance. However, such a morphology does not exist in nature.

### 2.2. Control Model

The longitudinal dynamics near hovering is governed by the Newton-Euler equations. Referring to Figure 2, Newton's equation reads

$$m\ddot{u} = X_u u + X_q q + mg\theta \quad (1)$$

where  $m$  is the mass of the robot,  $u$  is the velocity of the center of mass (CG),  $\theta$  is the pitch angle (assumed small, so that  $\sin \theta \simeq \theta$  and  $\cos \theta \simeq 1$ ) and  $q = \dot{\theta}$  is the pitch velocity.  $L$  is the lift (follower) force; at hovering its vertical component balances the gravity force  $L = mg$  and the component along the body axis  $X_B$  is  $mg\theta$ .  $X_u u + X_q q$  is the drag force acting at the center of drag (CD) along the body axis  $X_B$ .

The main damping mechanism is the flapping of the wings. The complex aerodynamic forces can be modelled by a point force  $f_d$  proportional to the velocity of the center of drag located  $z_d$  above the center of mass (Figure 2). The position of the center of drag is estimated at a quarter chord from the leading edge at mid-wing. The drag force is proportional to the velocity of the center of drag:

$$f_d = -K(u + qz_d) \quad (2)$$

with the constant  $K$  being a linear function of the flapping frequency.  $u$  is the axial velocity of the center of mass and  $q$  is the pitch angular velocity. This model was validated with a set of pendulum experiments and was found to be very accurate [6,17]. It follows that the constants appearing in Equation (1) are  $X_u = -K$  and  $X_q = -Kz_d$ .

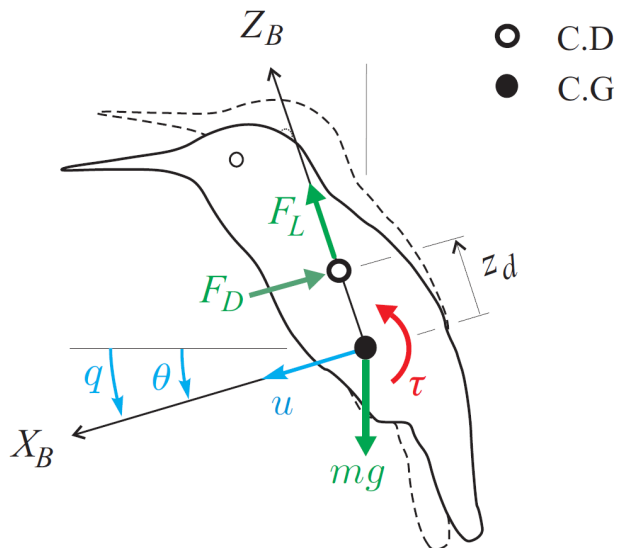


**Figure 2.** Longitudinal (pitch) model of the robot near hovering. Coordinate system, force and moment diagram.

Similarly, the rotary motion follows the Euler equation:

$$I_{yy}\dot{q} = M_u u + M_q q + \tau_a \quad (3)$$

where  $I_{yy}$  is the moment of inertia about the center of mass;  $M_u u + M_q q$  is the drag torque with  $M_u = -Kz_d$  and  $M_q = -K_q - Kz_d^2$ .  $M_q$  can be estimated also with a pendulum experiment (with the pendulum axis aligned on the center of mass). Direct and fairly accurate measurements of  $X_u$  and  $M_q$  are available while the cross coupling terms  $X_q$  and  $M_u$  result from a model and are less accurate; the distance  $z_d$  between the center of mass and the center of drag is not known accurately.

The aerodynamic control torque  $\tau_a$  results from the wing twisting obtained by the rotation of the control bars. The latter are operated by servos which can be modelled as first-order systems, so that the actual control torque  $\tau_a$  is related to the requested torque  $\tau$  (output of the controller) by

$$T\dot{\tau}_a + \tau_a = \tau \quad (4)$$

where  $T$  is the time constant of the servo. In state-space form, the cycle-averaged longitudinal dynamics read

$$\begin{bmatrix} \dot{u} \\ \dot{q} \\ \dot{\theta} \\ \dot{\tau}_a \end{bmatrix} = \begin{bmatrix} \hat{X}_u & \hat{X}_q & g & 0 \\ \hat{M}_u & \hat{M}_q & 0 & 1/I_{yy} \\ 0 & 1 & 0 & 0 \\ 0 & 0 & 0 & -1/T \end{bmatrix} \begin{bmatrix} u \\ q \\ \theta \\ \tau_a \end{bmatrix} + \begin{bmatrix} 0 \\ 0 \\ 0 \\ 1/T \end{bmatrix} \tau + \begin{bmatrix} d/m \\ t_p/I_{yy} \\ 0 \\ 0 \end{bmatrix} \quad (5)$$

where  $\hat{X}_u = X_u/m$  and  $\hat{M}_q = M_q/I_{yy}$  are always negative and  $\hat{X}_q = X_q/m$  and  $\hat{M}_u = M_u/I_{yy}$  are negative if  $z_d > 0$ , that is if the center of drag is above the center of mass, and positive if  $z_d < 0$ . The above equation includes the flapping drag noise  $d$  and the pitch flapping torque noise  $t_p$  that enter the system at the input. Time-histories of the lift  $L$ , the drag  $d$  and the pitch torque  $t_p$  have been studied in experiments reported in [11]. The signals are periodic but very complex, involving a lot of harmonic components and peak values at least one order of magnitude larger than their cycle-averaged values. For example, the RMS value of the aerodynamic torque  $t_p$  is 0.0273 N·m (2780 gr·mm) while the (cycle-averaged) control torque that can be achieved by the control bars is limited to 2 N·mm ( $\pm 200$  gr·mm).

Similar considerations apply to the lateral dynamics with significantly lower values of the drag and torque noise because of the symmetry.

### 3. Stabilization

In short, the axial dynamics of the robot can be written in the classical state space form

$$\dot{x} = Ax + B\tau + w \quad (6)$$

where  $x = (u, q, \theta, \tau_a)^T$ . The matrices  $A$  and  $B$  are given in Equation (5).  $w$  represents the system noise produced by the flapping of the wings,  $(d/m, t_p/I_{yy}, 0, 0)^T$ , as discussed above.

The open-loop longitudinal dynamics is unstable and the poles configuration (the eigenvalues of  $A$ ) depends strongly of the value of  $z_d$ . For  $z_d > 0$  (center of drag above the center of mass), the system has two unstable oscillatory poles and two poles on the negative real axis (blue  $\times$  in Figure 3). If one considers the system as a SISO system with the control torque  $\tau$  as input and the pitch angle  $\theta$  as output, the system can be stabilized with a PD compensator,  $-k_\theta(1 + T_q s)$ . This adds a zero in the open-loop system; Figure 3 shows the root locus as a function of the proportional gain  $k_\theta$ . The position of the closed-loop poles corresponding to  $T_q = 0.27$ ,  $z_d = 15$  mm and  $k_\theta = 192 \times 10^5$  is indicated in red [6].

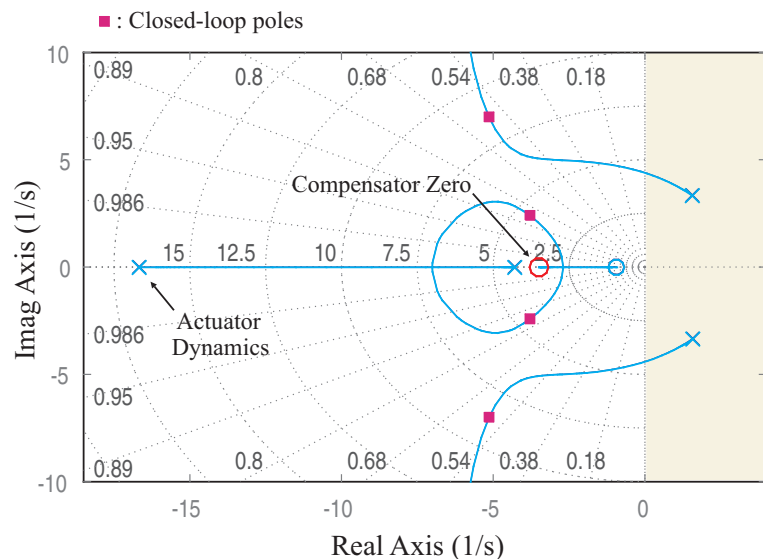


**Figure 3.** Root-locus plot trajectories as a function of the proportional feedback gain  $k_\theta$  for PD control of the robot  $\frac{\tau(s)}{\theta(s)} = -k_\theta(1 + T_q s)$  with  $T_q = 0.27$  and  $z_d = 15$  mm. The open-loop poles and zero are the blue  $\times$ . The red squares indicate the closed-loop poles location obtained with  $k_\theta = 192 \times 10^{-5}$ .

### 4. Attitude Estimation

The PD compensator discussed above looks satisfactory; however, the pitch angle  $\theta$  is not directly available because the IMU MEMS unit consists of three rate gyros measuring the roll-pitch-yaw angular velocity in the robot frame and the three components of the *specific acceleration*  $s = \mathbf{a} - \mathbf{g}$ , i.e., the absolute vector acceleration  $\mathbf{a}$  of the IMU unit minus the gravity vector  $\mathbf{g}$ .

#### 4.1. Output Equation

In hovering, the absolute acceleration  $\mathbf{a} = 0$  and the specific acceleration  $\mathbf{s} = (s_x, s_y, s_z)^T$  indicates the position of the gravity vector in the robot frame, from which the robot attitude (roll-pitch) can be calculated:

$$\phi = \text{Atan2}(-s_y, -s_z) \quad (7)$$

$$\theta = \text{Atan2}(-s_x, \sqrt{s_y^2 + s_z^2}) \quad (8)$$

For the 1-D model considered here, if the IMU is located at a distance  $z_a$  of the center of mass ( $z_a > 0$  if the IMU is above the center of mass and  $z_a < 0$  if it is below), the  $x$  and  $z$  components of the specific acceleration are, respectively,

$$s_x = \dot{u} + \dot{q} \cdot z_a - g \sin \theta \quad s_x \simeq \dot{u} + \dot{q} \cdot z_a - g\theta \quad (9)$$

$$s_z = +g \cos \theta \simeq g. \quad (10)$$

At hovering,  $\theta = \arctan -s_x/s_z \simeq -s_x/s_z$  and, because the component  $s_z$  is subject to the intense periodic fluctuation of the lift force,  $\theta \simeq -s_x/g$  may be a more accurate estimator.

From the foregoing discussion, we conclude that the important components of the IMU outputs are  $s_x$  (the  $x$  component of the accelerometer) and  $q$  (the  $y$  component of the gyro). Considering the system equation, Equation (5), the output equation relating the sensor output  $y = (s_x, q)^T$  to the state vector  $x = (u, q, \theta, \tau_a)^T$  reads

$$\begin{bmatrix} s_x \\ q \end{bmatrix} = \begin{bmatrix} (\hat{X}_u + \hat{M}_u z_a) & (\hat{X}_q + \hat{M}_q z_a) & 0 & z_a/I_{yy} \\ 0 & 1 & 0 & 0 \end{bmatrix} \begin{bmatrix} u \\ q \\ \theta \\ \tau_a \end{bmatrix} \quad (11)$$

in short,  $y = Cx$ . Let us consider two different ways of dealing with the output signal to estimate the pitch attitude angle  $\theta$ .

#### 4.2. Complementary Filter

The gyros of the IMU unit provide the pitch rate  $q = \dot{\theta}$  that can be integrated to obtain an estimator of  $\theta$ . However, it is well known that gyros are prone to drift. This can be alleviated by high-pass (HP) filtering.

On the other hand, we have just seen that, at hovering, the MEMS accelerometers provide another estimator,  $\theta_a \simeq \arctan -s_x/g \simeq -s_x/g$ . The sensitivity to the intense high-frequency flapping noise can be alleviated by low-pass filtering (LP).

The idea in the Complementary Filter (CF) consists of combining the output of the two filters above; assuming second order Butterworth filters, the estimator reads

$$\hat{\theta} = \frac{s^2}{s^2 + \sqrt{2}\omega_c s + \omega_c^2} \cdot \left(\frac{1}{s}\right) \cdot q + \frac{\sqrt{2}\omega_c s + \omega_c^2}{s^2 + \sqrt{2}\omega_c s + \omega_c^2} \cdot \theta_a \quad (12)$$

where  $\omega_c = 2\pi f_c$  is the corner frequency of the complementary filter, delimiting the frequency ranges where the accelerometer and the gyro are more reliable. Note that the sum of the two filters, HP + LP, is an all-pass filter.

The system can be looked at as a SISO system with input  $\theta_d$  and output  $\theta$ ; its block diagram is shown in Figure 4. The return loop involves three low-pass filters, at  $f_g$  on the gyro output, at  $f_s$  on the accelerometer output, and  $f_c$  in the complementary filter, respectively.  $f_g$  is particularly important, because its output  $\dot{q}_g$  is directly used in the construction of the control torque  $\tau$ ; it has a direct impact on the stability margins. Extensive numerical studies [11] have shown that  $f_g = 8$  Hz offers a good compromise between stability and noise rejection. The frequencies  $f_s$  (accelerometer output) and the complementary filter corner frequency  $f_c$  are less critical; they have been selected  $f_s = 2$  Hz and  $f_c = 0.1$  Hz.

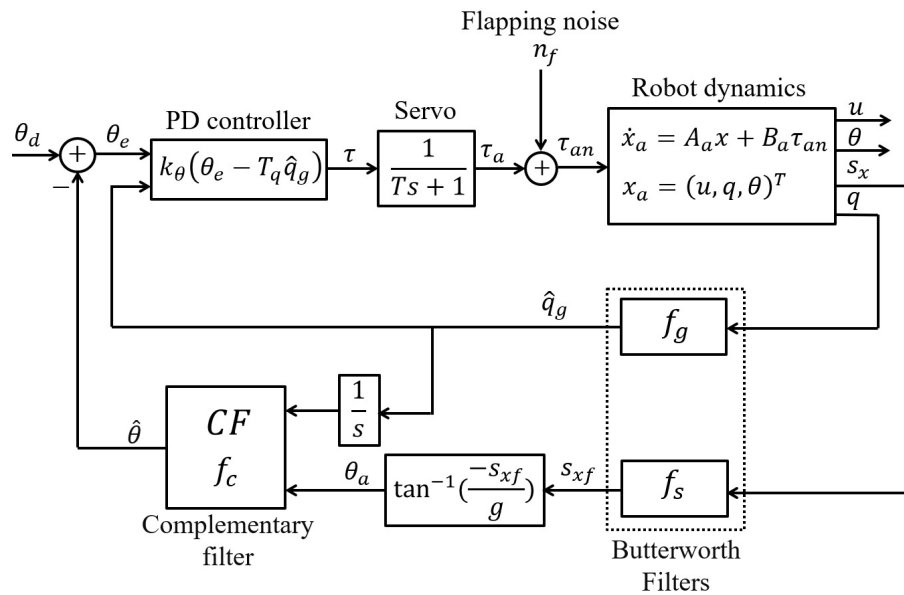


**Figure 4.** Block diagram of the longitudinal stability control loop with a complementary filter.  $\tau$  is the requested control torque,  $\tau_a$  is the position of the servo actuator acting on the control bars and  $\tau_{an}$  is the actual torque produced by the flapping wings, including the periodic noise components.

#### 4.3. Full-State Dynamic Observer

The central assumption in the complementary filter is that of hovering, that is, the absolute acceleration is  $\mathbf{a} = 0$ , so that the direction of the gravity vector in the robot frame can be extracted from the accelerometer signal. Since the robot is subjected to a strong flapping noise, an alternative approach consists of including the robot dynamics in the attitude estimation; this approach is advocated by [18] for spacecraft applications. A solution is given by a full-state dynamic observer (*Luenberger observer*) provided that a reasonably accurate linear state space model is available, Equations (6) and (11) in this case. The reconstructed state  $\hat{x}$  is solution of

$$\dot{\hat{x}} = A\hat{x} + B\tau + L(y - C\hat{x}) \quad \hat{x}(0) = 0 \quad (13)$$

This equation assumes that the model is accurate; the error  $e = x - \hat{x}$  follows the equation

$$\dot{e} = (A - LC)e + w - Lv \quad (14)$$

where  $L$  is the observer gain matrix, chosen to achieve adequate filtering properties of the IMU signals from the gyro and the accelerometer. According to the *separation principle*, the closed-loop poles consist of two decoupled sets, corresponding to the full-state feedback regulator (PD in this case) and the full-state observer; the closed-loop stability is guaranteed provided the eigenvalues of  $A - LC$  have negative real parts. The observer gain matrix may be obtained by pole placement or as a Kalman-Bucy filter, in short, *Kalman Filter* (KF), assuming that the plant noise  $w$  and the sensor noise  $v$  are white noise of given covariance matrices,  $W$  and  $V$ , respectively. This approach is followed here.

#### 4.4. Kalman Filter

From measurements reported in [11], the variance of the drag noise and the pitch torque noise are estimated:  $\sigma^2(d/m) \simeq 2000 \text{ (N/kg)}^2$  and  $\sigma^2(t_d/I_{yy}) \simeq 200,000 \text{ (N/kg.m)}^2$  (the components of the plant noise are expressed in different units; in SI units, their ratio is 100). The sensor noise covariance matrix may be estimated from the zero-acceleration output of the accelerometers and the zero-rate output of the gyros, available from the data sheet of the IMU sensor,  $0.30 \text{ m/s}^2$  and  $0.085 \text{ rad/s}$ , respectively, leading to  $\sigma^2(s_x) \simeq 0.09 \text{ (m/s}^2)^2$

and  $\sigma^2(q) \simeq 0.008 \text{ (rad/s)}^2$ , respectively. Thus the ratio  $\sigma^2(s_x)/\sigma^2(q) \simeq 10$ . Figure 5 shows the block diagram of the longitudinal stability control loop with a full-state dynamic observer.

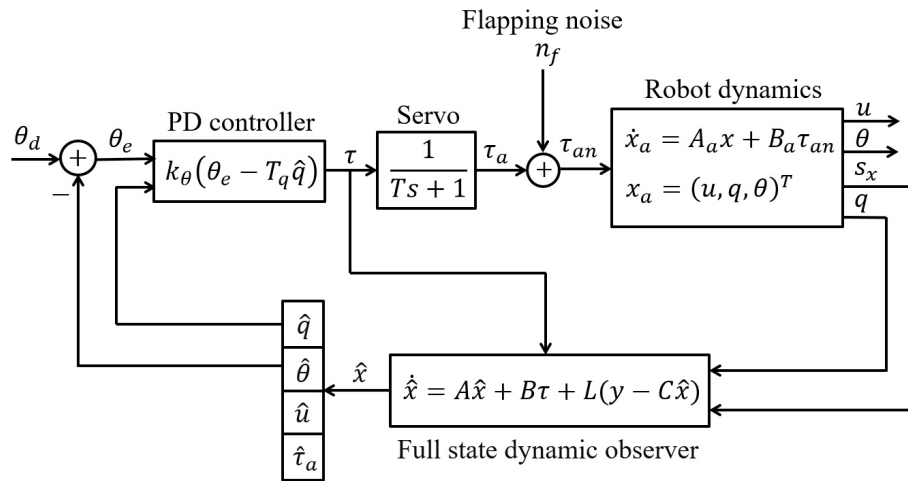


**Figure 5.** Block diagram of the longitudinal stability control loop with a full-state dynamic observer. The symbols have the same meaning as in the previous figure.

According to the foregoing discussion, we *assume* the following form for the plant noise  $W$  and the sensor noise  $V$  covariance matrices:

$$W = \text{diag}(2, 200, 0, 0) \quad V = \alpha \times \text{diag}(10, 1) \quad (15)$$

where  $\alpha$  is a design parameter. A small value of  $\alpha$  indicates that low noise measurements may be trusted. Note that only the ratio between  $V$  and  $W$  matters (multiplying both matrices by a scalar leads to the same gain matrix  $L$ ). The measurement noise acts as an excitation in the observer error Equation (14), amplified by the observer gain matrix ( $Lv$ ); as a result, noisy measurements require moderate gains in the observer.

Figure 6 shows the observer poles for three values of  $\alpha$ , 1, 10 and 100, respectively. The poles of the PD regulator shown earlier in Figure 3 are also shown. The value of  $\alpha = 1$  has been used in what follows.

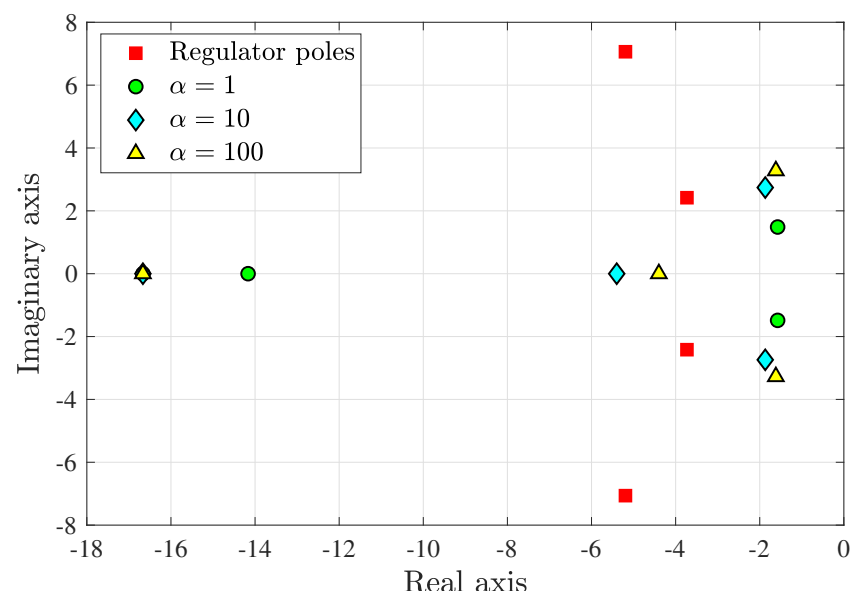


**Figure 6.** Observer poles for  $\alpha = 1, 10$  and  $100$  (the pole on the left side of the real axis is common to all values of  $\alpha$ ). The regulator poles of Figure 3 are also shown with red squares.

## 5. Flight Tests

The control strategy explained for stabilizing the pitch ( $X$ ) axis is applied also for the roll ( $Y$ ) axis with appropriate values of the parameters of the Kalman filter (the model parameters for  $X$  and  $Y$  are slightly different, due to differences in the various drag coefficients appearing in the control model). The Complementary Filter (CF) and the Kalman Filter (KF) attitude reconstruction have been implemented in the control board. Attitude stabilization of the robot has been achieved successfully with both methods as illustrated by the video [19]. Figure 7 compares the reconstructed pitch angle and pitch rate of the two filters for a short spell of a stationary flight when the stabilization feedback loop is based on the Kalman Filter. Notice that the accelerometer output has a RMS amplitude of  $4.1\text{ g}$ , while a pitch angle of  $0.1\text{ rad}$  corresponds to an horizontal component of the gravity acceleration of  $0.1\text{ g}$ . This means that the signal to noise ratio is of the order of  $1\%$ , which is quite challenging. We have observed that the reconstructed signal from the KF is systematically lower than that reconstructed from the CF, and the same trend has been observed when the stabilization loop is based on CF rather than KF. However, both filters successfully stabilize the robot and no significant visual difference is observed as illustrated in the video [19].

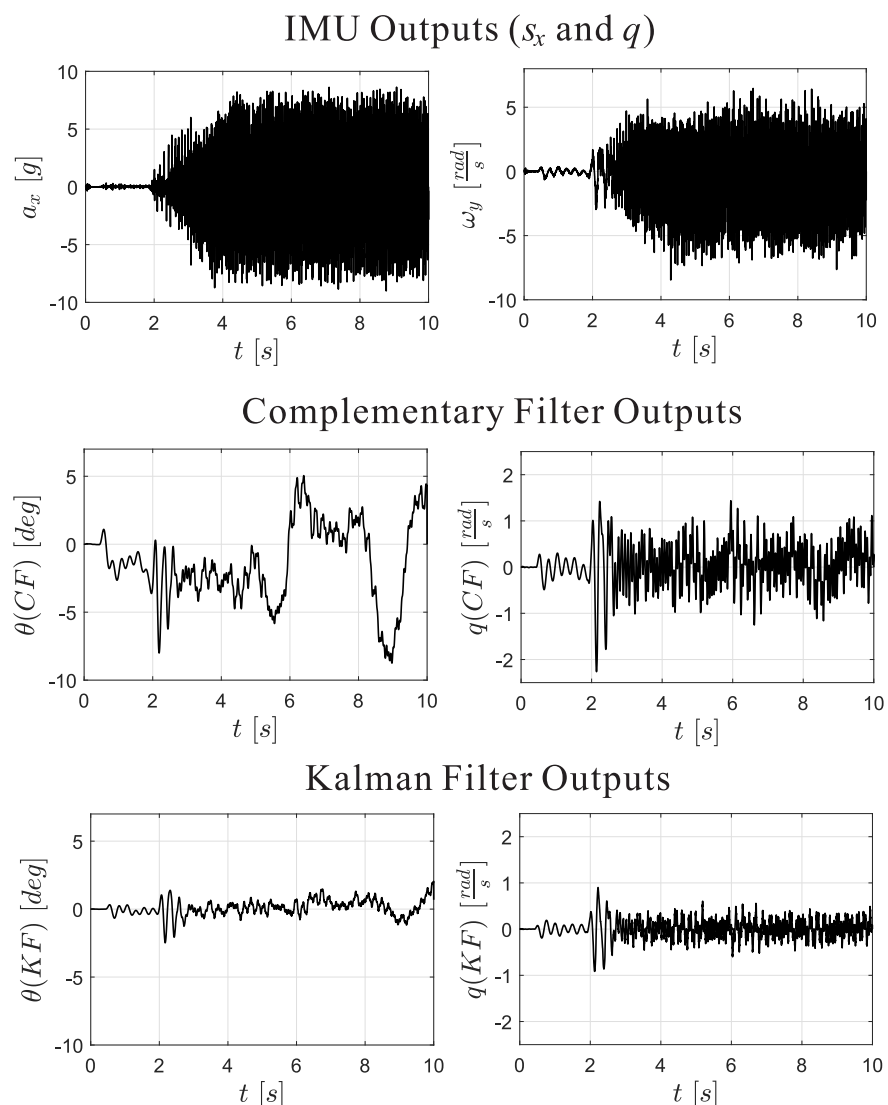


**Figure 7.** Comparison of the outputs of the Complementary Filter (CF:  $\hat{\theta}, \hat{q}_g$  in Figure 4) and the Kalman Filter (KF:  $\hat{\theta}, \hat{q}$  in Figure 5) in a short interval of a stationary flight ( $\theta_d = 0$ ) when the stabilization feedback loop is based on the Kalman Filter output. The upper figures refer to the IMU outputs ( $s_x, q$ ).

### 5.1. Station Keeping

When the references of the pitch and roll control loops are set to  $\theta_d = 0$ , the robot does not remain exactly at the same place but slowly drifts away from its starting position due to small inaccuracies in the IMU calibration, the strong flapping noise, the imperfect symmetry between the forward and backward strokes, etc. [19]. The Kalman filter reconstructs the full state that includes the forward velocity  $u$  (and the lateral velocity  $v$ ). If the signal reconstruction is good enough, a cascaded control of the linear velocity may be implemented as shown in Figure 8. The compensator  $C(s)$  transforms the velocity error into a pitch angle demand  $\theta_d$  with a P+I compensator:

$$C(s) = g_u \frac{s + z_u}{s} \quad (16)$$

where the parameters  $g_u$  and  $z_u$  have been selected after numerical simulations to provide adequate stability margins [11], and finally adjusted from flight tests. The proposed strategy looks fairly straightforward, but it was not obvious that it would work in practice, given the severe flapping noise affecting the IMU sensor. The flight tests have shown that it works as one can see one the short video [20]. The left side of Figure 9 compares trajectories of the center of mass of the robot with (in red) and without (in blue) velocity control measured by an external tracking system. The right side of the figure shows similar measurements conducted earlier when the velocity used in the feedback was that reconstructed from the external tracking system [6]. This figure shows similar performances of the two approaches; the on-board measurements allows to keep the robot within a circle with a radius of about one wingspan.

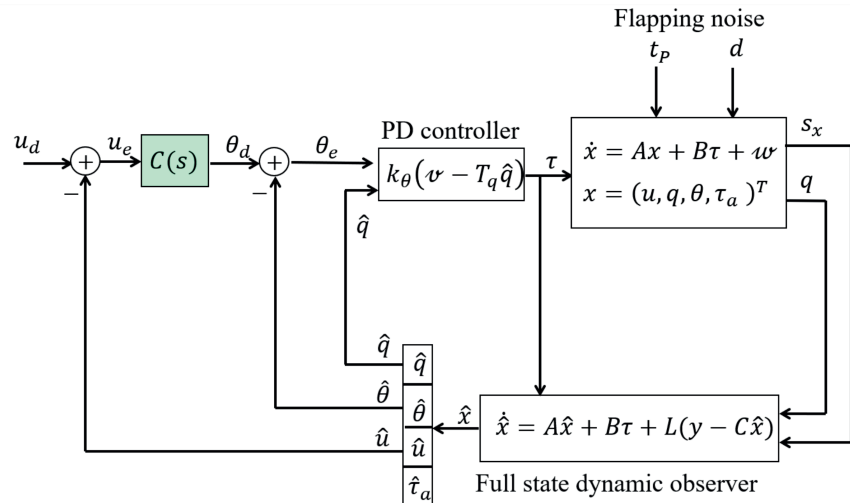


**Figure 8.** Cascaded control on the linear velocity  $u$ . The flapping noise includes the drag  $d$  and the pitch torque  $t_p$ .

### 5.2. Yaw Control, Trajectory Generation

The control configuration shown in Figure 8 is exactly the configuration needed to generate the axial and lateral components of the robot trajectories. However, a careful observation of the videos reveal that the robot slowly rotates about the yaw axis. This is due to the fact that, to speed-up the research, the current versions of our demonstrator do not include an actuator to control the yaw axis, which is necessary for a full control of the trajectory.

The yaw axis is naturally stable (it is damped by the flapping of the wing); its control has been investigated in [21]. Unlike the pitch and roll torques which are generated by lift modulation, the yaw torque results from differential drag obtained by modifying slightly in opposite directions the central position of the left and right control bars. Once this step is achieved, the magnetometer included in one of the two IMU units in the control board

can be used to steer the front axis of the robot and generate trajectories. This step remains to be performed.

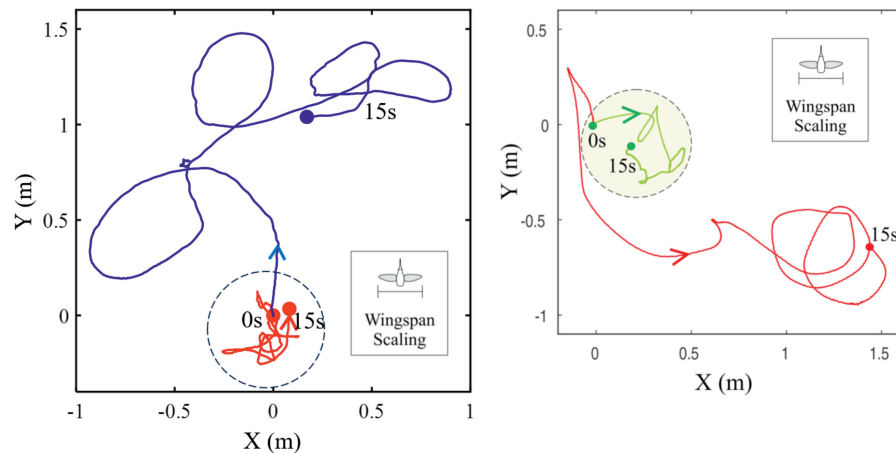


**Figure 9.** Comparison of trajectories with and without velocity control. Left: velocity control based on the reconstruction from the on-board sensor and Kalman filter. Right: velocity control based on an external tracking system [6].

## 6. Endurance Flight

Two prototypes have been built and tested, that differ by the mechanical structure of the flapping wing mechanism (both have the same kinematics), the gear ratio  $G$  of the gearbox between the d.c. motor and the flapping mechanism and the wing size  $W$  (which affects the lift-frequency relationship and the pitch and roll control moments), Table 1. Two sets of batteries have been considered with the characteristics of Table 2. In each case, two batteries are connected in series. All tests were performed with the same d.c. motor with the characteristics (at room temperature) of Table 3.

**Table 1.** Characteristics of the prototypes considered in this study.

Prototype Number	Flapping Mechanism	Gearbox Ratio $G$	Wing Size $W$ (mm)	Weight $L$ (gr)	Flapping Frequency $f$ (Hz)
P1	String	28.9	88	22	18
P2	Gear	39	81	22.6	19

**Table 2.** Characteristics of the batteries.

Battery Number	Reference	Capacity (mAh)	Discharge Rate	Weight (gr)	Max. Current (A)
B1	Hyperion G5 LiPo	70	25C–30C (50C burst)	2.26	1.75–2.1
B2	Honcell	95	15C	2.3	1.425

**Table 3.** Characteristics of the d.c. motor.

Producer	Weight (gr)	$R(\Omega)$	$k (10^{-4} \text{V.s})$	$R/k^2 (\times 10^8)$
Micronwings	3.51	0.76	7.18	0.0147

The two prototypes were first tested on a load cell with an external power supply; the voltage  $e$  and current  $I$  necessary to achieve a lift equal to the weight were measured (Table 4). The average current needed for the control board and the two attitude control servos was also estimated to 0.19 A, so that the total current supplied by the battery is

$i = I + 0.19$  A. Table 4 also provides estimates of the electrical power of the motor  $P_e = e \times I$ , the heat power  $P_h = RI^2$  and the mechanical power (necessary to produce the lift and overcome the internal friction in the mechanism and the motor)  $P_m = P_e - P_h$ .

**Table 4.** Flight characteristics of the robots.

Prototype Number	Operating Voltage $e$	Operating Current $I$	Electrical Power $P_e$	Heat Power $P_h$	Mechanical Power $P_m$
P1	3.2	1.12	3.58	0.95	2.63
P2	3.92	0.97	3.80	0.715	3.08

Figure 10 shows the discharge curve of two batteries B1 connected in series. The open circles indicate the data from the manufacturer for  $i = 1.2$  A and the continuous lines correspond to the best-fit Shepherd model [22] for the requested current of the prototypes P1 and P2 (the requested current  $i$  is obtained by adding the current needed for the board and attitude servos to the values given in the third column of Table 4,  $i = I + 0.19$  A). The minimum voltage to operate the control board and the servos is 6 V, so the expected operating time  $T_0$  with a constant current is obtained when the Shepherd model drops below 6 V.

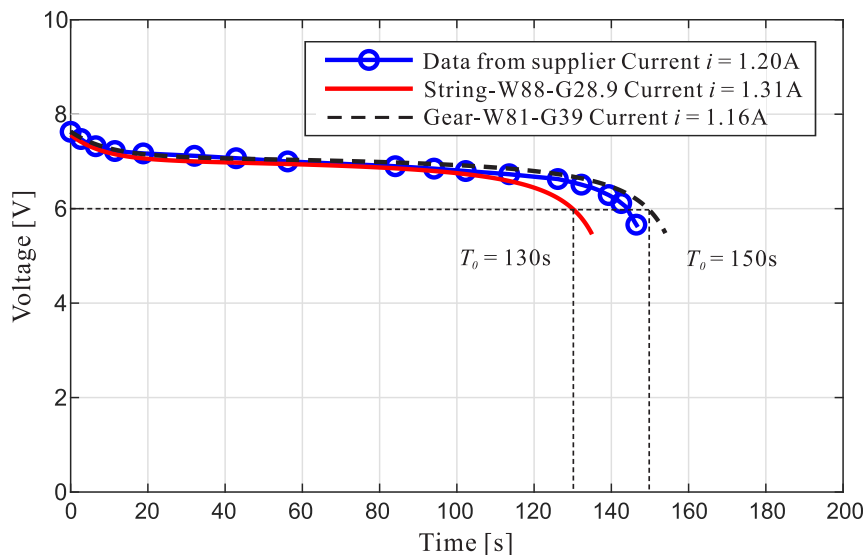


**Figure 10.** Discharge curve of two batteries B1 in series for a the discharge rate of 1.2 A (data from manufacturer) and the best-fit Shepherd model. The other curves correspond to the Shepherd model for the discharge currents of the two prototypes.

In the flight tests, the operator adjusts the duty factor of the PWM of the main motor in order to keep a nearly constant altitude (lift equal to weight). When the available voltage at the battery  $v$  is larger than the requested voltage  $e$ , the duty factor  $\mu$  of the PWM of the d.c. motor (i.e., the fraction of time when the full available voltage is applied) is set to  $\mu = e/v$ . It follows that the total flight time may be estimated by

$$T = \int_0^{T_0} \frac{v}{e} dt \quad (17)$$

Table 5 summarizes the results for the two prototypes and the two sets of batteries.  $T_0$  is the constant current discharge time obtained from Shepherd's model, and  $T$  is the flight time estimate from Equation (17).  $T_f$  is the actual flight time measured. P1-B1 refers to the string mechanism with the first set of batteries; the flight stopped after 106 s because of overheating of the main motor (the energy of the battery was not exhausted). As a result, the flight P1-B2 became useless and was canceled. The flight P2-B1 (gear mechanism) lasted  $T_f = 168$  s, well below the estimated  $T = 265$  s; at least part of the discrepancy can be

attributed to the fact that the set of batteries B1 had been used for a long time. The flight P2-B2 is the longest so far,  $T_f = 265$  s (nearly 4 min 30 s).

**Table 5.** Estimated and measured flight time, specific power  $P_m/L$ .

Prototype Battery	Shepherd $T_0$	Estimated $T$ Equation (17)	Actual Flight $T_f$	$P_m/L$ (W/kg)	Remark
P1-B1	130 s	279 s	106 s	119	Overheating
P1-B2	-	-	-	-	-
P2-B1	150 s	265 s	168 s	136	Old batteries
P2-B2	NA	NA	265 s	136	Longest flight

From Table 5, one sees that prototype P1 is subject to overheating in spite of a specific power  $P_m/L = 119$  W/kg while the prototype P2 flies longer with a specific power of 136 W/kg. The reason lies into the following relation between the heat power  $P_h$  and the mechanical power  $P_m$  [10]:

$$P_h = RI^2 = \frac{R}{k^2} \cdot \frac{1}{G^2} \cdot \left(\frac{P_m}{2\pi f}\right)^2 \quad (18)$$

The first term is motor characteristics (Table 3), the second depends on the gear ratio  $G$  and the third one depends on the flapping frequency  $f$ . According to this equation,  $P_h \sim P_m^2(Gf)^{-2}$ . On the other hand, previous studies have shown that, for a given lift, the mechanical power  $P_m$  is to a large extent independent on the wing size (see Figure 6 of [10]). This means that a larger gear ratio and smaller wings (leading to a larger flapping frequency) will reduce heat production. The excess value of the specific power of the gear mechanism as compared to the string mechanism hints that internal friction could be reduced by more accurate components and careful assembly.

## 7. Conclusions

The attitude reconstruction of a hovering flapping wing robot has been analyzed with a complementary filter and a full-state dynamic observer. Both methods have been successfully implemented and tested, in spite of the high noise environment due to the flapping of the wings. In addition, it was found that the full-state observer allows the reconstruction of the forward and the lateral velocities needed for station keeping and full control of the robot trajectory.

Endurance tests were conducted with two different robot configurations; the maximum flight time observed is 265 s (4 min 30 s) in spite of some parasitic friction in the geared flapping mechanism. Future studies will be devoted to the control of trajectories and increasing the flight time of the robot.

**Author Contributions:** Conceptualization, A.P., H.W., Y.F. and L.W.; software, Y.F., L.W. and H.W.; test and validation, H.W., L.W. and Y.F.; writing—original draft preparation, A.P.; writing—review and editing, A.P. and Y.F.; supervision, A.P. and E.G. All authors have read and agreed to the published version of the manuscript.

**Funding:** This research received no external funding.

**Institutional Review Board Statement:** Not applicable.

**Informed Consent Statement:** Not applicable.

**Data Availability Statement:** Data are contained within the article.

**Acknowledgments:** The authors wish to thank Gert Geboers from Dekimo n.v. for his careful work in the manufacturing of the control board and his availability and help in the initial phase of programming. Many thanks also to Lorenzo Brancato, enthusiastic MSc student of Politecnico di Milano, who contributed to the programming and the early tests in the project during his Erasmus internship at ULB.

**Conflicts of Interest:** The authors declare no conflicts of interest.

## Abbreviations

The following abbreviations are used in this manuscript:

ARM	Advanced RISC Machine
CD	Center of drag
CF	Complementary Filter
CG	Center of mass
DARPA	Defense Advanced Research Projects Agency
HP	High Pass filter
IMU	Inertial Measurement Unit
KF	Kalman Filter
LP	Low pass filter
MEMS	Micro Electro Mechanical System
NA	Non Available
PD	Proportional plus Derivative
PI	Proportional plus Integral
PWM	Pulse Width Modulation
RMS	Root Mean Square
SI	International System Units
SISO	Single Input Single Output

## References

1. Xiao, S.; Hu, K.; Huang, B.; Deng, H.; Ding, X. A Review of Research on the Mechanical Design of Hoverable Flapping Wing Micro-Air Vehicles. *J. Bionic Eng.* **2021**, *18*, 1235–1254. [[CrossRef](#)]
2. Ward, T.A.; Rezadad, M.; Fearday, C.J.; Viyapuri, R. A Review of Biomimetic Air Vehicle Research: 1984–2014. *Int. J. Micro Air Veh.* **2015**, *7*, 375–394. [[CrossRef](#)]
3. Keenon, M.T.; Klingebiel, K.R.; Won, H.; Andriukov, A. Development of the nano hummingbird: A tailless flapping wing micro air vehicle. In Proceedings of the 50th AIAA Aerospace Sciences Meeting including the New Horizons Forum and Aerospace Exposition, Nashville, TN, USA, 9–12 January 2012; pp. 1–24.
4. Phan, H.V.; Park, H.C. Insect-inspired, tailless, hover-capable flapping-wing robots: Recent progress, challenges, and future directions. *Prog. Aerosp. Sci.* **2019**, *111*, 100573. [[CrossRef](#)]
5. Phan, H.V.; Aurecianus, S.; Au, T.K.L.; Kang, T.; Park, H.C. Towards Long-Endurance Flight of an Insect-Inspired, Tailless, Two-Winged, Flapping-Wing Flying Robot. *IEEE Robot. Autom. Lett.* **2020**, *5*, 5059–5066. [[CrossRef](#)]
6. Roshanbin, A. Design and Development of a Tailless Robotic Hummingbird. Ph.D. Thesis, Université Libre de Bruxelles, Dept Control Engineering and System Analysis, Bruxelles, Belgium, September 2019.
7. Roshanbin, A.; Altartouri, H.; Karasek, M.; Preumont, A. COLIBRI: A Hovering Flapping Twin-Wing Robot. *Int. J. Micro Air Veh.* **2017**, *9*, 270–282. [[CrossRef](#)]
8. Roshanbin, A.; Abad, F.; Preumont, A. Kinematic and Aerodynamic Enhancement of a Robotic Hummingbird. *AIAA J.* **2019**, *57*, 4599–4607. [[CrossRef](#)]
9. Colibri Maiden Flight. Available online: <https://www.youtube.com/watch?v=-5-o9tvbzI> (accessed on 3 February 2024).
10. Preumont, A.; Wang, H.; Kang, S.; Wang, K.; Roshanbin, A. A Note on the Electromechanical Design of a Robotic Hummingbird. *Actuators* **2021**, *10*, 52. [[CrossRef](#)]
11. Farid, Y.; Wang, L.; Brancato, L.; Wang, H.; Wang, K.; Preumont, A. Robotic Hummingbird Axial Dynamics and Control near Hovering: A Simulation Model. *Actuators* **2023**, *12*, 262. [[CrossRef](#)]
12. Greenwalt, C.H. *Hummingbirds*; Dover: New York, NY, USA, 1990.
13. Van Breugel, F.; Regan, W.; Lipson, H. From Insects to Machines. *IEEE Robot. Autom. Mag.* **2008**, *15*, 68–74. [[CrossRef](#)]
14. Ristroph, L.; Ristroph, G.; Morozova, S.; Bergou, A.J.; Chang, S.; Guckenheimer, J.; Wang, Z.J.; Cohen, I. Active and passive stabilization of body pitch in insect flight. *J. R. Soc. Interface* **2013**, *10*, 20130237. [[CrossRef](#)] [[PubMed](#)]

15. Teoh, Z.E.; Fuller, S.B.; Chirarattananon, P.; Pérez-Arcibia, N.O.; Greenberg, J.D.; Wood, R.J. A Hovering Flapping-Wing Microrobot with Altitude Control and Passive Upright Stability. In Proceedings of the 2012 IEEE/RSJ International Conference on Intelligent Robots and Systems, Vilamoura-Algarve, Portugal, 7–12 October 2012; pp. 3209–3216.
16. Karásek, M.; Muijres, F.T.; De Wagter, C.; Remes, B.D.; De Croon, G.C. A tailless aerial robotic flapper reveals that flies use torque coupling in rapid banked turns. *Science* **2018**, *361*, 1089–1094. [[CrossRef](#)] [[PubMed](#)]
17. Altartouri, H.; Roshanbin, A.; Andreolli, G.; Fazzi, L.; Karásek, M.; Lalami, M.; Preumont, A. Passive stability enhancement with sails of a hovering flapping twin-wing robot. *Int. J. Micro Air Veh.* **2019**, *11*, 1756829319841817. [[CrossRef](#)]
18. Yang, Y.; Zhou, Z. Attitude determination: With or without spacecraft dynamics. *Adv. Aircr. Spacecr. Sci.* **2017**, *4*, 335–351.
19. CF and KF Stabilization Loop. Available online: <https://youtu.be/ZCN5RK5Thb0> (accessed on 3 February 2024).
20. Station Keeping. Available online: <https://youtu.be/53DJ0rtебKk> (accessed on 3 February 2024).
21. Roshanbin, A.; Preumont, A. Yaw control torque generation for a hovering robotic hummingbird. *Int. J. Adv. Robot. Syst.* **2019**, *16*, 1–14. [[CrossRef](#)]
22. Shepherd, C.M. Design of Primary and Secondary Cells-Part 2. An Equation Describing Battery Discharge. *J. Electrochem. Soc.* **1965**, *112*, 657–664. [[CrossRef](#)]

**Disclaimer/Publisher's Note:** The statements, opinions and data contained in all publications are solely those of the individual author(s) and contributor(s) and not of MDPI and/or the editor(s). MDPI and/or the editor(s) disclaim responsibility for any injury to people or property resulting from any ideas, methods, instructions or products referred to in the content.